Bayesian landmark identification in medical images

Mohammad-Reza Siadat[*1,2], Hamid Soltanian-Zadeh[2,3], Farshad Fotouhi[1], Kost Elisevich[4]

[1]Department of Computer Science, Wayne State University, Detroit, MI 48202, USA
[2]Radiology Image Analysis Lab., Henry Ford Health System, Detroit, MI 48202, USA
[3]Electrical and Computer Engineering Dept., University of Tehran, Tehran 14395, Iran
[4]Dept. of Neurosurgery, Henry Ford Health System, Detroit, MI 48202, USA

ABSTRACT

This paper presents a generic and unified method to identify a set of anatomical landmarks of interest within the medical image domains. Landmark identification is important as it provides us with: 1) initial information for registration, 2) navigation and retrieval guidance through the image data, 3) initial models for segmentation, and 4) valuable (though rough) information about the organs/structures of interest. The proposed method initially uses a supervised learning procedure and then improves itself based on the Bayes' theory. The procedure at the first step requires an expert to define a rough roadmap passing through a set of high-contrast landmarks (milestones), and eventually reaching at the structure of interest. The expert is asked to mark the milestones as desired points and a few points around them as undesired points, respectively. Then we estimate Gaussian models for the marked points by which the optimal search area for each desired landmark is determined. The search areas estimated at this step are considered as the segments of the statistical roadmap. An additional set of statistical models along with the above ones are used to form a set of rules to evaluate the points being found during the search procedure. The points that satisfy the rules will be recognized as the landmarks of interest. As the above method is being applied on a set of new patients/cases, a set of valid landmarks of interests becomes available. This new piece of information is then being used to modify the current statistical roadmap based on the Bayes' theory. We have applied the proposed method on T1-weighted brain MRI of 10 epileptic patients to find the landmarks of the hippocampus. In our experiment, six patients formed the training set, and we observed one-step iteration of the Bayesian modification. The method made no false alarms. The overall success rate (average of sensitivity and specificity) of the algorithm was 83.3% with an accuracy of 99.2%. In localizing the hippocampus, the proposed method (with almost perfect results) was 600 times faster than the mutual information registration (with poor and partly wrong results).

Keywords: Bayes' Theory, Medical Image Registration, Segmentation, Brain Structure Localization and Identification.

1. INTRODUCTION

Quantitative analysis of the anatomical structures on MRI scans is recommended for human[1] and animal[2] brain studies. Such analysis requires the anatomical structures to be segmented. Manual segmentation is labor-intensive, costly, requires an expert operator, and is not reproducible. A study in our institution showed a large variability for the hippocampi volumes when manually segmented by two experts (intra-subjects variability) on MRI studies of 11 patients. The percent difference between the hippocampi volumes determined by the two experts ranged from 3% to 133% and averaged at 57%[3]. The mentioned problems are limiting factors in inter-institutional as well as intra-institutional quantitative studies. As the result, extraction of quantitative information from MRI is currently done by a limited number of institutions.

Automatic procedures are expected to solve the above problems, thereby making it possible for most medical institutions to benefit from quantitative information of the anatomical structures. However, segmentation of many anatomical structures with conventional methods, e.g., edge detection/tracking, thresholding, or region growing is not possible. This is due to the fact that such structures have relatively low contrast or/and multiple or discontinuous/missing edges on MRI scans. Warping an atlas to the patient's brain MRI is one of the methods proposed in recent years[4]. Alternatively, deformable models have been proposed for the segmentation of these structures[5-7].

The atlas mapping/warping is among the methods that have been widely used for human brain segmentation[8-12]. These methods are usually categorized among model-based segmentation methods. For relatively small and highly

[*] Correspondences to: msiadat@cs.wayne.edu, siadat@rad.hfh.edu, hamids@rad.hfh.edu. http://radiologyresearch.org

Medical Imaging 2004: Image Processing, edited by J. Michael Fitzpatrick, Milan Sonka, Proceedings of SPIE Vol. 5370 (SPIE, Bellingham, WA, 2004)
1605-7422/04/$15 doi: 10.1117/12.535754

variable structures like the hippocampus, these methods do not usually provide good results due to their sensitivity to the imperfections involved in the registration and warping steps. Hsu, et al., have reported[11] that the reliability of automatic volumetry (using warping method) depends on the selection of the hippocampal template (atlas). Moreover, the warping/mapping methods are computationally inefficient since they deform the whole image dataset to match the atlas. The more degrees of freedom in the matching procedure, the more accurate (in theory) the warping, and the more time consuming the procedure. In many cases we are just interested in one single structure (e.g., hippocampus), yet we have to match the whole brain. Therefore, the atlas warping is neither sufficient nor efficient for the segmentation of many small-sized structures with high variability in their shapes/sizes. The deformable models require an initial shape (state) from which they start and evolve until they come to a final shape (rest state). Leaving the definition of the initial shape to the user may result in low productivity and low reproducibility[13]. Using atlas mapping/warping to define the initial shape, as proposed in references[5,14-17], is insufficient for small-sized and highly variable structures (e.g., the hippocampus).

This paper presents a knowledge-based method, which uses the Bayesian information fusion theory to localize small structures on the human brain MRI. As a complicated application, we apply the proposed method to the localization and identification of the hippocampus. During the training phase an expert is asked to design a roadmap passing through high-contrast structures like the lateral ventricles by which we can find several landmarks around the hippocampus from different viewpoints. Then we ask the expert to mark the landmarks of interest for each segment of the roadmap as the desired points and a few points close to the desired points with similar characteristics as undesired points. Having the desired and undesired points marked on several slices of the training set, we estimate statistical models for desired and undesired landmarks. Using these models, we estimate the search areas on which the landmarks of interest are most likely to be found when looking from their corresponding viewpoints. We propose a search method to look for a point with a particular intensity or neighboring connectivity within the determined search area. The search takes place on binary images of white matter (WM), gray matter (GM), or cerebrospinal fluid (CSF) that presents the landmark of interest the best. We design a set of rules using the statistical models of the landmarks of interest coded in a knowledge-based system. The knowledge-based system performs an approximate reasoning to evaluate the landmarks found during the information extraction step. The points recognized valid define an initial polygon for the hippocampus. To modify the estimated models, the search areas, and eventually the statistical roadmap, we incorporate the information of the newly evaluated and approved landmarks in the model as soon as the number of such cases matches that of the cases participating in the estimation of the current model. This information fusion pretty much obeys the Bayesian theory. The proposed method is very fast since it just deals with a few landmarks of interest and it is very focused on the task we are interested in. We claim that this method is closer to the way a human expert does the job. That is no expert (neuro-radiologist) looks through the whole image dataset to segment the hippocampus. Instead, the experts look for some landmarks of interest that lead to the structure of interest. They may further verify the identified structure by some well-defined and high contrast neighboring structures. Details of the proposed method are described in Section 2. Experimental results are presented in Section 3.

2. METHOD

The proposed method consists of two main steps: 1) information extraction and 2) information analysis, discussed in Sections 2.1 and 2.2, respectively. The information extraction step locates a set of anatomical landmarks. The information analysis step analyzes the extracted information (landmarks) to determine whether or not the structure of interest is identified/localized correctly and accurately.

2.1. Information Extraction

When localizing an anatomical structure, especially with low contrast and missing boundaries, the experts tend to look at the well-defined neighboring structures with high contrast to ensure that they have targeted the correct spot. This observation brings up the notion of making a roadmap to get to a desired structure/landmark/destination. A roadmap simply consists of a starting point and a few milestones with pre-specified directions/segments taking us from one milestone to the next. We add to this the idea of having several roadmaps to reach the final destination instead of being dependent on just one. Having multiple roadmaps provides extra clues to verify the final destination.

Unlike the geographical maps, in an anatomical map the road from one landmark to the next one can not be deterministically defined since it varies from one person/patient to the other. So, we have to make a statistical map to optimize the probability of detection vs. the false alarm rate (sensitivity vs. specificity). There is an approximate geometrical position for each anatomical structure/landmark in which it would reside and thus can be looked for and

found. An approximate relative spatial relationship does also exist among the anatomical structures. The above two postulations make it possible to build a statistical brain roadmap to localize the brain structures.

We use the expert-marked landmarks of six epileptic patients (as the training set) to estimate the statistical models (distributions) for the desired and undesired landmarks in Section 2.1.1. The undesired landmarks are located close to the desired ones with similar features to those of the desired landmarks. However, they are not the landmarks we would like to end up with. We also explain how the Bayesian method is utilized to fuse the information born, as the method is being applied on new cases, into the current statistical models/roadmap. In Section 2.1.2, using the estimated models, we determine the optimal search area for each desired landmark as the road segment from one milestone to the next. In Section 2.1.3 we describe the search algorithm by which the landmarks of interest are searched for. The above three steps will be then applied on our specific application: hippocampus localization, in Section 2.1.4. Note that we use the fuzzy C-Means clustering algorithm to generate binary images of CSF, GM, and WM where the search algorithm takes place on. However, since it is not the focus of this paper we do not present it in details.

2.1.1. Statistical models of landmarks of interest and Bayesian modification of the models

To estimate the statistical models of the landmarks, an expert has marked them on over 70 MRI slices of six patients (training set). Then a 2D normal (Gaussian) density function is estimated for each landmark as follows:

$$N(x,y)=\frac{1}{2\pi\sqrt{|Det(C)|}}\exp\left(-\tfrac{1}{2}[x-m_x \quad y-m_y]\,C^{-1}\begin{bmatrix}x-m_x\\ y-m_y\end{bmatrix}\right) \tag{1}$$

where C and $[m_x\ m_y]$ are the covariance matrix and the mean vector of the marked points, respectively. Fig. 1 depicts an instance of the marked landmarks, Fig. 1(a), and the sum of their corresponding estimated normal density functions (when undesired models are considered negative), Fig. 1(b).

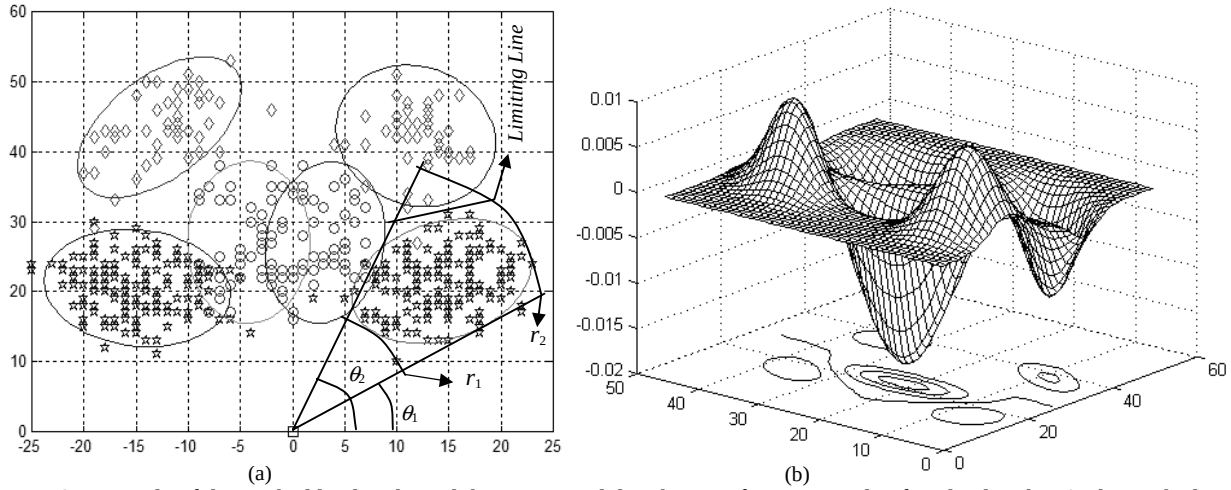

Fig. 1. An example of the marked landmarks and their estimated distributions for an example of six landmarks. a) The marked points with the iso-countors drawn where only 5% of the volume under the estimated distribution function left outside. b) The 3D plot of the sum of the estimated Gaussian distributions where the undesired models are considered to be negative.

Using the Bayes' theory, we iteratively modify the statistical models of the desired landmarks. In the Bayesian formula (2), the current statistical model of each landmark is considered to be the prior, $P(M)$. So, during the first iteration, the initial models produced by the supervised procedure is going to be considered as the prior. Then using the new landmarks introduced by the set of new patients and validated by the proposed knowledge-based system (to be fully described in the following sections), we compute the likelihood, $P(D|M)$, and eventually the posterior, $P(M|D)$. Note that we do not modify the model unless the number of patients in new dataset matches the total number of cases by which the prior has already been estimated. At the first iteration, the number of patients participating in the prior determination equals the number of members in the training set, which is six in our case. So, as we modify the current model(s), the number of participating cases becomes doubled for the next iteration. Since we use only the landmarks that already been validated by the current model, the estimated distribution of the new data is going to be conditional on the current model, i.e., $P(D|M)$, which is nothing but the likelihood. As mentioned, the prior is a normal distribution, N_p. We

estimate a normal distribution for the likelihood, N_L, since we did not find any conjugate prior for the normal distribution. As the result, the posterior, $\overline{\overline{N_P N_L}}$, will not be a normal distribution. On the other hand, the estimation of the search area discussed in the next section requires normal distribution. So we take an extra step to estimate the best normal distribution that approximates the posterior. We estimate this normal distribution by calculating the mean vector and covariance matrix of the posterior as shown in Formulae (3).

$$P(M \mid D) = \frac{P(M) \times P(D \mid M)}{P(D)} \tag{2}$$

$$m_x = Ex = \int_{-\infty}^{\infty} x \left(\int_{-\infty}^{\infty} \overline{\overline{N_P N_L}} dy \right) dx, \quad m_y = Ey = \int_{-\infty}^{\infty} y \left(\int_{-\infty}^{\infty} \overline{\overline{N_P N_L}} dx \right) dy, \quad \sigma_{xx} = E x^2 = \int_{-\infty}^{\infty} \int_{-\infty}^{\infty} x^2 \overline{\overline{N_P N_L}} dxdy,$$

$$\sigma_{xy} = E xy = \int_{-\infty}^{\infty} \int_{-\infty}^{\infty} xy \overline{\overline{N_P N_L}} dxdy, \text{ and } \sigma_{yy} = E y^2 = \int_{-\infty}^{\infty} \int_{-\infty}^{\infty} y^2 \overline{\overline{N_P N_L}} dxdy \text{ where } \overline{\overline{N_P N_L}} \stackrel{\Delta}{=} \frac{N_P \times N_L}{\int_{-\infty}^{\infty} \int_{-\infty}^{\infty} N_P \times N_L \, dxdy} \tag{3}$$

The flowchart in Fig. 2. depicts the iterative method explained above. Fig. 2(a) shows an iso-contour of the unknown Ground Truth (GT) distribution that we would like to eventually estimate in dash-line. In this figure the iso-contours are drawn in such a way that only 5% of the volume under the distribution surface leaves outside. The points generated by the GT distribution are shown in this figure as well. Note that the points reside inside the iso-contour of the prior are marked by squares and used to estimate the likelihood. Fig. 2(b),(c) show the iso-contours of the posterior and the estimated normal distribution of it, respectively. As shown in Fig. 2(c) the model produced by one-step Bayesian modification fits much better to the ground truth compared to the prior.

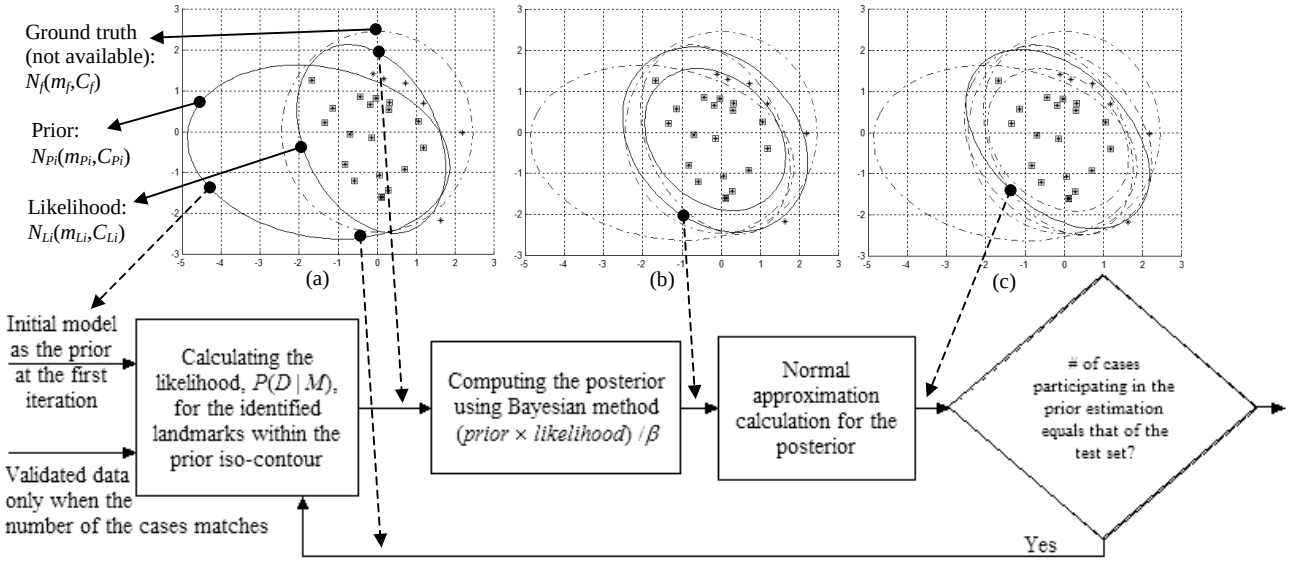

Fig. 2. The iterative Bayesian modification method.

2.1.2. Definition of search areas

The search area is usually characterized by a viewpoint, two angles of view, and two far- and near-zone arcs. The viewpoint is usually determined in the overall roadmap design procedure. The search regions are derived from the statistical models of the structures (shown in Fig. 1(a)) and more specifically from the iso-contours of the models. The volume under the distribution function inside the iso-contour represents the likelihood of residing the landmark inside the region. We call this likelihood "confidence level," as a lower bound at which the detection rate of the search algorithm is set. We use an optimization procedure[18] to calculate the z-value at which the density function can be cut to

produce the iso-contour for a given confidence level. We set the confidence level at 95% for all structures either desired or undesired throughout this research. The objective function we minimize is as follows:

$$Obj(z) = \left| \iint_{inside\ iso-contour\,(z)} N(x,y)dxdy \; - \; 0.95 \right|^2 . \tag{3}$$

We use the determined iso-contours and the viewpoint to define the search area. In the simplest case, the view angles are the tangential lines to the iso-contour from the viewpoint. The search near- and far-zone limits are the tangential arcs to the iso-contour with the viewpoint as the center. Finding the tangential line and arc has analytic solutions.

The search area determined above does sometimes partially cover the iso-contour of a neighboring undesired structure. There are even cases where the desired and undesired iso-contours are intersecting. We take care of these cases by adding limiting lines as being described in the example below. Assume that we would like to determine a search area for the points/landmarks depicted by pentagram points in Fig. 1(a) from the viewpoint marked by the square point (located at [0 0]). Since there is no undesired structure at the lower-right side of the desired structure, θ_1 can be determined by the tangential line to the iso-contour shown in Fig. 1(a). Also, there is no undesired structure between the viewpoint and the desired structure, so we choose the tangential arc with radius r_1, as the near-zone limit. For the other view angle (θ_2) the iso-contours of the desired and undesired structures (pentagram and circles) are intersecting. In such cases the "tangential line" solution leads the algorithm to a low specificity, i.e., large number of false alarms, which is not desirable. We propose an optimal solution in the sense that the specificity and sensitivity are balanced.

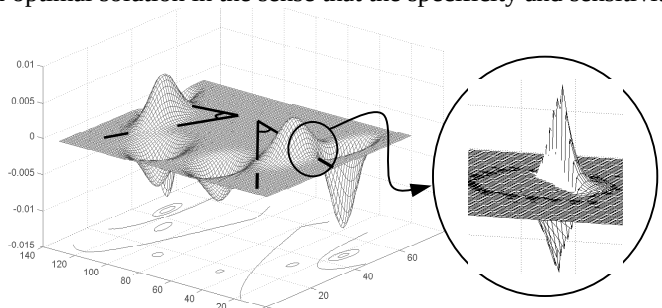

(a) (b)

Fig. 3. (a) The 3D illustration of the overall map made up of sum of all density functions where undesired models are considered to be negative. The viewpoints and the search angles are also shown. (b) The portions of the desired and undesired models outside and inside the search angle, respectively, in a zoomed-in view.

Fig. 3(a) shows a 3D illustration of an overall distribution map made up of the sum of all probability density functions where undesired models are considered to be negative. Fig. 3(b) shows portions of the desired and undesired density functions outside and inside the search angle, respectively, as positive and negative edges. The positive edge corresponds to the probability of missing the desired structure (1 − sensitivity). The negative edge corresponds to the probability of false alarm (1 − specificity). The specificity and sensitivity are balanced when the positive and the negative portions shown in Fig. 3(b) cancel each other out. Therefore, we minimize the objective function in formula (3) to obtain an optimal solution

$$Obj(\theta) = \left| \iint_{search\ angle\ side} N_u(x,y)dxdy \quad + \iint_{outside\ the\ search\ angle} N_d(x,y)dxdy \right|^2 \tag{4}$$

where N_d and N_u are the desired and undesired models, respectively, and θ is the angle of view (θ_2 in Fig. 1(a)). The positive and negative portions shown in Fig. 3(b) correspond to the first and the second terms in (4), respectively. Very similarly the limiting line shown in Fig. 1(a) is determined. The difference is that we optimize the objective function to estimate not only the angle/slope but also the line interception (h): $Obj(\theta, h)$.

2.1.3. Search method (traversing search area)

In general, the search is performed from an initial radius relative to a viewpoint and expands toward a final boundary (r_1 and r_2 in Fig. 4(a), respectively). For each radius all the pixels between two angles of view (θ_1 and θ_2 in Fig. 4(a)) are

examined before decreasing/increasing the search radius. In the simplest case, the search looks for a pixel with a particular "intensity." To decrease the sensitivity to the image noise, we may search for a pixel with specific spatial connectivity constraint (e.g., 8-neighbor connectivity). For example, in Fig. 4(a) an active (dark) point with at least 7 active neighbors in an 8-nearest neighborhood is searched and found. Once a point satisfies the search condition, an enhanced morphological algorithm based on Finding Connected Component (FCC)[19] is invoked. Using one of the structuring elements shown in Fig. 5, FCC is applied to grow the connected regions directionally and eventually reach to an anatomical landmark.

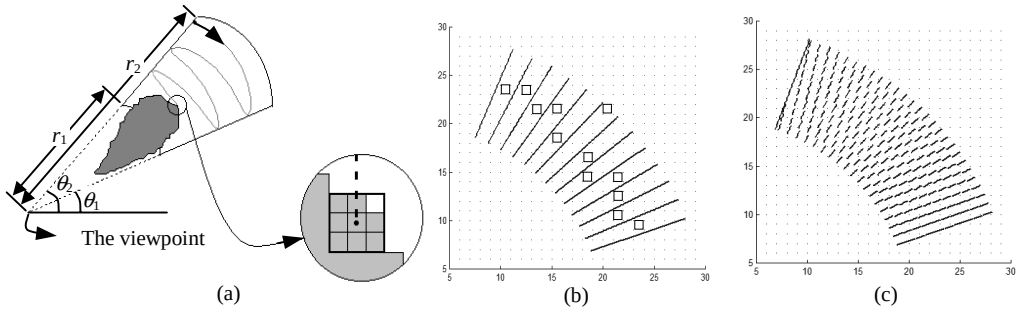

(a) (b) (c)

Fig. 4. a) The search method mimicking the emission of the radii of light/sight, b) fixed angle step-size and the possibility of missing pixels during the procedure of traversing the search area. The squares present some of the missing pixels, c) determining the angle step-size adaptively leaves no pixel untouched/unexamined.

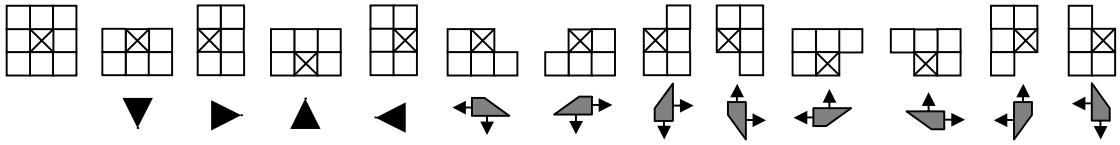

(a) (b) (c) (d) (e) (f) (g) (h) (i) (j) (k) (l) (f)

Fig. 5. The structuring elements of the finding connected components (FCC) algorithm modified to grow directionally.

To ensure all of the pixels in a search region are viewed, we determine the angle step-size as a function of the radius. The worse case scenario happens for the pixels with sides perpendicular to the direction of the view angle. Therefore, the angle step-size should be smaller than the angle introduced by the pixel-side segment and the coordinates of the viewpoint, i.e., $\Delta\theta \leq \arctan(1/r)$ where r is the radius connecting the viewpoint to the pixel being examined. A search with a fixed angle step-size either leads to inefficiency (each pixel is examined more than one time) or fails to examine all the pixels (unexamined pixels are marked with squares in Fig. 4(b)). Unlike the case with a fixed angle step-size, the adaptive method (Fig. 4(c)) proposed here provides a relatively efficient search and guarantees to examine all the pixels in the search area.

2.1.4. Application of proposed roadmap to hippocampus

The anatomical structures of interest participating in the roadmap to the hippocampus include: 1) A point on the brain midline inferior to the most superior point of the head by half of the head width as the starting point, 2) the lateral ventricles, 3) the insular cortex, and finally the destination which is the hippocampus. The proposed search approach first finds the lateral ventricles on the CSF binary images. A morphological algorithm (FFC) is utilized to extract the whole ventricle structure and locate particular landmarks on lateral and third ventricles. Using the lateral landmarks of the lateral ventricles, we initiate a search to identify the landmarks on the superior borders of the hippocampi. From the superior landmark of the hippocampus, search regions are defined to identify the medial inferior landmark of the hippocampus and the insular cortex. The medial inferior landmark of the insular cortex is located using the FCC algorithm. This landmark defines the search region to identify lateral landmarks of the hippocampi. Using the lateral and the inferior points of the hippocampus a search from the superior landmark of this structure is performed to find a fourth point (somewhere between the lateral and inferior points) of this structure. The searches for the superior and the lateral landmarks of the hippocampus and the insular cortex take place on GM binary images. The search for the inferior and the fourth point of the hippocampus is performed on WM binary images.

Fig. 6(a) shows the background and CSF (BK&CSF) binary image on which three lines at the superior and the lateral limits of the head have been drawn. These three lines determine the width and the most superior limits of the head

providing the coordinates of the starting point of the search (point-1 in Fig. 6(b)). The desired and undesired points are shown in Fig. 6(b). The distribution of the desired and undesired points for about 50 images of the training set are shown and the iso-contours (at 95% confidence level) and the search areas are schematically depicted in Fig. 6(c).

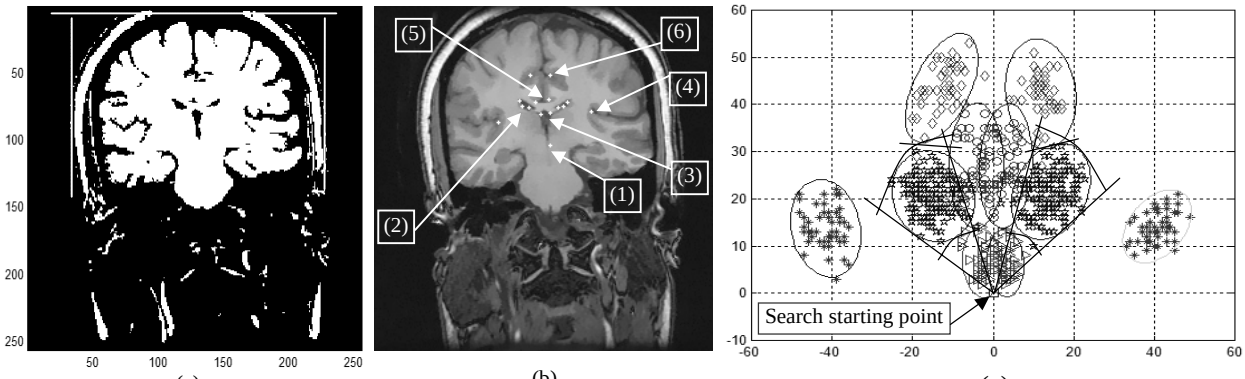

(a) (b) (c)

Fig. 6. a) A BK&CSF binary image where the lateral and superior limits of the head is determined which provides us with the starting point of the search. b) The expert landmark identification for lateral ventricles when looking from the starting point (point-1); the lateral ventricles (point-2) as the desired landmark; the superior corners of the third ventricle (point-3), the Sylvian fissure (point-4), and lateral points of the callosal sulcus (point-5) and the eingulate sulcus (point-6) as undesired landmarks. c) The distribution of the desired and undesired landmarks with the iso-contours drawn at 95% confidence level.

When an active point is found, we employ the FCC algorithm with the structuring element shown in Fig. 5(a) to segment the whole structure connected to the found point as the left/right lateral ventricle. Then we find the superior, inferior, lateral, and medial landmarks of the segmented structure. The lateral landmarks are used as the starting viewpoints when looking for the superior landmarks of the hippocampus. The search angles and radii along with the limiting lines are summarized in Table I.

The undesired landmarks/structures around the superior limits of the hippocampus are the medial limits of the insular cortex and the lateral inferior limits of the hypothalamus. We search for an active point with at least 5 active neighbors in its 8-nearest neighborhood on the GM binary images. The search angles and radii are summarized in Table I.

The search for the medial inferior landmark of the insular cortex is initiated from the superior points of the hippocampus (Fig. 7(a) point-4). The undesired landmarks/structures are the lateral points of the hypothalamus and the medial points of the superior-middle temporal gyral interface (SMGTI), shown in Fig. 7(a) as point-1 and point-3, respectively. The target landmark/structure is the medial inferior limits of the insular cortex shown in Fig. 7(a) as point-2. We search on the GM binary images for an active point with at least 6 active neighbors in its 8-nearest neighborhood. Fig. 7(b) illustrates the search performed at the left side of the brain. Note that the limiting lines of the left and the right sides are defined in two different coordinate systems, i.e., left and right superior landmarks of the hippocampus coordinates system. The search angles and radii along with the limiting lines are summarized in Table I.

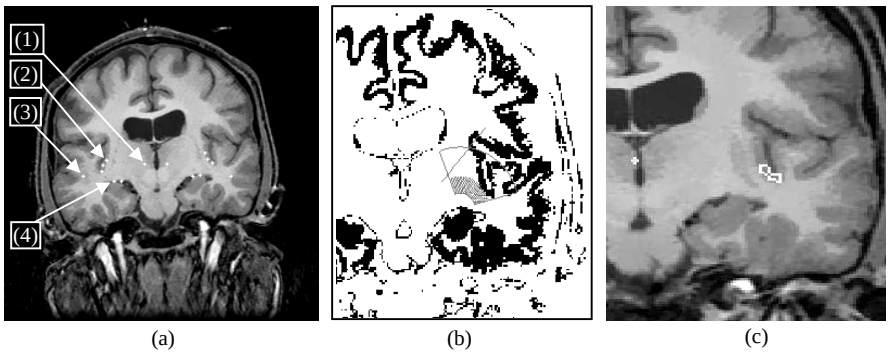

(a) (b) (c)

Fig. 7. a) The manual landmark identification of the desired and undesired structures when looking from the superior points of the hippocampus (point-4). The medial point of the insular cortex (point-2) is the desired points. The lateral limits of the hypothalamus (point-1) and the medial limits of the SMGTI (point-3) are undesired landmarks. b) The search performed on a GM binary image to

find an active (black) point with at least six neighboring active points in its 8-nearest neighborhood. c) The region connected to the point found in (b) grown downward by applying directional FCC.

When a point of the insular cortex is found we extend its connected region downward to find the inferior landmark of this structure. This landmark is used as the viewpoint to search for the lateral landmarks of the hippocampus. To reach the inferior point, we use FCC with the structuring element shown in Fig. 5(b). Fig. 7(c) illustrates an instance of the grown region.

TABLE I. Summary of each segment (search area) of the roadmap estimated based on the supervised procedure.

View point	Target point	θ_1	θ_2	r_1 (pixel)	r_2 (pixel)	Limiting line
Starting point	Left lateral ventricle	36.9°	72.9°	38	15	$y = 17/60\ x + 27$
Starting point	Right lateral ventricle	148°	108.4°	38	15	$y = -17/60\ x + 27$
Left lateral ventricle	Left superior hippocampus	–30.9°	–92°	10	35	-
Right lateral ventricle	Right superior hippocampus	–149.2°	–88°	10	35	-
Left superior hippocampus	Left insular cortex	14.9°	111.3°	8	32	$y = 49/41\ x + 26$
Right superior hippocampus	Right insular cortex	76.5°	165.1°	8	32	$y = -49/41\ x + 26$
Left insular cortex	Left lateral hippocampus	–163.8°	–66.8°	5	20	-
Right insular cortex	Right lateral hippocampus	–16.2°	–71.6°	5	20	-
Left superior hippocampus	Left inferior hippocampus	–48.37°	–108.44°	2.5	17.5	$y = \pm(45/77)\ x - 18$
Right superior hippocampus	Right inferior hippocampus	–63.95°	–120.96°	2.5	17.5	$y = \pm(45/20)\ x - 32$
Left superior hippocampus	Left fourth point	See the text		8	32	-
Right superior hippocampus	Right fourth point	See the text		8	32	-

The next segment of the roadmap starts from the medial inferior landmarks of the insular cortex toward the lateral landmarks of the hippocampus. The superior limits of the PFGI and the medial limits of the SMGTI are considered undesired landmarks. The search for the lateral landmark of the left hippocampus is performed for an active point with at least 3 active neighbors in its 4-nearest neighborhood on GM binary images. The search angles and radii are summarized in Table I.

The hippocampus looks like a peninsula of gray matter extended horizontally in white matter on the coronal T1-weighted MR images. To find the inferior landmarks of the hippocampus a search is initiated from the superior point of this structure. The white matter extended adjacent to the lateral limits of the PFGI is considered undesired, as well as the lateral limits of the peduncular. The search is performed for an active point with at least 7 active neighbors in its 8-nearest neighborhood on WM binary images. The search angles and radii along with the limiting lines are summarized in Table I.

For the fourth point of the hippocampus, we compute the median bisector of the edge connecting the inferior and the lateral points of the hippocampus in a triangle formed by these two points and the superior point of the hippocampus. We search from the superior point of the hippocampus in the direction of the median bisector with ±2° deviations. The search is performed for an active point with 2 active neighbors in its 4-nearest neighborhood. The search radii are summarized in Table I.

2.2. Information Analysis

We employ fourteen rules as the core of the proposed knowledge-based. The approach to design the rules using the statistical roadmap and two examples of the rules are presented in Section 2.2.1. The approximate reasoning proposed to combine the results produced by the rules applied on the extracted information is discussed in Section 2.2.2.

2.2.1. Proposed Rules

Each rule in the knowledge-based system generates an intermediate confidence factor (*ICNF*). An *ICNF* does usually address a particular abstract concept associated with the high-level object(s) of the roadmap such as the symmetry properties of the superior landmark of the hippocampus. We define three categories of rules based on: (*i*) absolute locations of the landmarks in the brain; (*ii*) relative locations of the landmarks compare to the other structures within the brain; and (*iii*) general symmetry of the brain. The first category is based on our first postulation that the brain landmarks have absolute ballpark locations on the slices presenting the structure of interest. Furthermore, this ballpark location can be statistically modeled (in a coordinate system built on the starting point of the search defined in Section 2.1). So we estimate statistical models for absolute locations of the landmarks of interest through manual landmark identification very similar to what discussed in details in the information extraction section. Fig. 8(a) depicts the points marked and the

iso-contours of the models estimated in this regard. As before, the iso-contours are determined at 95% confidence level that sets the probability of detection of the associated rules at 95%. The models shown in Fig. 8(a) demonstrate the absolute locations of the landmarks of interest in a coordinate system with the first point of search as its origin. If a landmark is found in an unexpected region, i.e., outside of the iso-contour, the confidence of the system in correct identification of the landmark decreases.

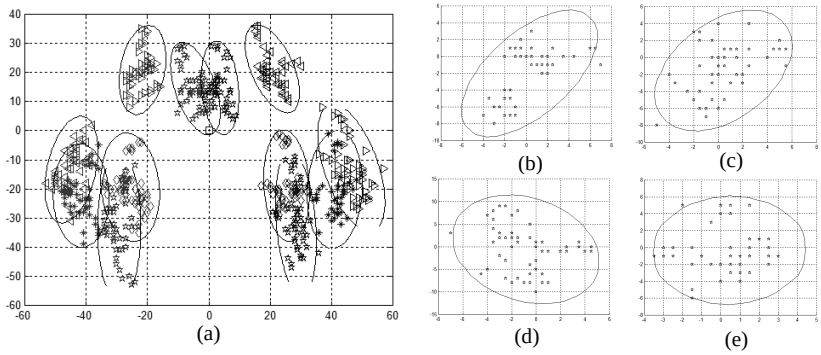

Fig. 8. a) The absolute coordinates of the lateral and medial points of the lateral ventricles (pentagrams and triangles, respectively), the superior, lateral, and inferior points of the hippocampus (diamonds, stars, and pentagrams, respectively), and the medial inferior points of the insular cortex (triangles). All the points are given in a coordinate system built on the search starting point (define in Section 2.1) as the origin. The iso-contours are drawn at 95% confidence level. (b)-(e) The deviations in *y*-coordinate for each pair of a landmark at the left and right hemisphere vs. the deviation of the average of the corresponding x-coordinates from the brain midline, b) the lateral, c) the inferior landmarks of the hippocampus, d) the medial inferior points of the insular cortex, e) the lateral landmarks of the lateral ventricles.

The second category considers the location of a brain structure relative to the other structures. In this case, a particular landmark is expected to be superior, inferior, medial, or lateral relative to another landmark. These qualitative expectations are converted to quantitative measures based on the statistical models (partly) shown in Fig. 8(b) as well as the ones derived in the information extraction section.

The third category is based on *general* symmetry of the brain. If MR images are acquired at coronal or axial directions/cross sections (or a combination of these two directions), the symmetry feature will be observed relative to the midplane. If there is a rotation toward the sagittal direction, this feature will not be valid any more. Abnormalities may also generate asymmetries in MR images. It should be mentioned that the symmetric property that we base some of the rules on is a *relative* concept and it does not require that one side to be an exact mirror projection of the other. We materialize this relative symmetry concept in the proposed rules based on the statistical models derived here and partly shown in Fig. 8(b)-(e).

Examples of Rules

We formally design the rules based on the models estimated so far instead of considering the meaning of them. However, when a rule is designed, one may assign it a meaning. We discuss the details of two rules, RULE-1 and RULE-10, which are examples of the absolute and symmetric rules, respectively. RULE-1 evaluates the superior landmarks of the hippocampi. *ABS*(.) is the absolute value function. (*SupHippo_RX*, *SupHippo_RY*) and (*SupHippo_LX*, *SupHippo_LY*) are the coordinates of the right and left superior points of the hippocampus, respectively. *Brn_CntrY* is the y-component of the search starting point defined in Section 2.1. The thresholds of 0, 38, 33, and 68 in the condition (antecedent) of the rule are the superior and inferior limits and the minimum and maximum horizontal (*x*-) distances of the iso-contours determined by the distribution models corresponding to the superior points of the hippocampus shown in Fig. 8(a). The *ELSE* part of the rule performs a soft transition from its neutral state to its denial state (from the score 0 to −100). The transient strip is 10 pixels wide and this width is going to be the same for most of the other rules.

Due to the general symmetric geometry of the brain with respect to the brain midplane, it is expected that the corresponding landmarks at the left and right brain hemispheres satisfy the following conditions: 1) the horizontal *x*-coordinates average around midline, 2) the vertical *y*-coordinates are not significantly different. We assume that the search starting point is on the brain midplane, therefore, the "horizontal *x*-coordinates averages of the symmetrically located structures" are supposed to be around the *x*-coordinate of the search starting point. The term "not significantly different" is interpreted for each case based on the statistical models estimated here and partly shown in Fig. 8(b)-(e).

For instance, for the inferior points of the hippocampus the corresponding model, the iso-contour in Fig. 8(c), suggests that the left and right landmarks may not be more than 9 pixels away in their *y*-coordinates.

For the deviation of the horizontal average from the search starting point, it is expected to be no more than 6 pixels. This is implemented in RULE-10, where (*InfHippo_RX*, *InfHippo_RY*) and (*InfHippo_LX*, *InfHippo_LY*) are the coordinates of the right and left inferior landmark of the hippocampus, respectively.

RULE-10

DifY = *InfHippo_RY* – *InfHippo_LY*
AVR = *Brn_CntrX* – (*InfHippo_RX* + *InfHippo_LX*)/2

IF *DifY* < 6 & *DifY* > –9 & *AVR* < 6 & *AVR* > –5
THEN *InfH_ICNF* = 100
ELSE
BUFF = 0;
IF *DifY* > 6
BUFF = $(BUFF^2 + (20 \times (DifY - 6))^2)^{0.5}$
END
IF *DifY* < –9
BUFF = $(BUFF^2 + (20 \times (DifY + 9))^2)^{0.5}$
END
IF *AVR* > 6
BUFF = $(BUFF^2 + (20 \times (AVR - 6))^2)^{0.5}$
END
IF *AVR* < –5
BUFF = $(BUFF^2 + (20 \times (AVR + 5))^2)^{0.5}$
END

InfH_ICNF = 100 – *BUFF*

IF *InfH_ICNF* < 0
InfH_ICNF = 0
END
END

RULE-1:

SuH_bndL = *SupHippo_LY* – *Brn_CntrY*
SuH_bndR = *SupHippo_RY* – *Brn_CntrY*
SuH_DifX = *ABS*(*SupHippo_RX* – *SupHippo_LX*)

IF *SuH_bndL* > 38 & *SuH_bndR* > 38 & *SuH_bndL* < 0
& *SuH_bndR* < 0 & *SuH_DifX* > 33 & *SuH_DifX* < 68
THEN *BndSH_ICNF* = 0
ELSE
BUFF = 0
IF *SuH_bndL* > 38
BUFF = $(BUFF^2 + (10 \times (SuH\_bndL - 38))^2)^{0.5}$
END
IF *SuH_bndL* < 0
BUFF = $(BUFF^2 + (10 \times (SuH\_bndL))^2)^{0.5}$
END
IF *SuH_bndR* > 38
BUFF = $(BUFF^2 + (10 \times (SuH\_bndR - 38))^2)^{0.5}$
END
IF *SuH_bndR* < 0
BUFF = $(BUFF^2 + (10 \times (SuH\_bndR))^2)^{0.5}$
END
IF *SuH_DifX* > 68
BUFF = $(BUFF^2 + (10 \times (SuH\_DifX - 68))^2)^{0.5}$
END
IF *SuH_DifX* < 33
BUFF = $(BUFF^2 + (20 \times (SuH\_DifX - 33))^2)^{0.5}$
END

BndSH_ICNF = –*BUFF*

IF *BndSH_ICNF* < –100
BndSH_ICNF = –100
END
END

2.2.3. Total *CNF* Calculation

The intermediate confidence factors, *ICNF*'s, are used to compute the overall confidence factor, the total *CNF*. If the total *CNF* is greater than a pre-specified threshold, the slice is determined to contain the hippocampus. In addition, the landmarks found around the hippocampus are assessed to be accurate enough (valid). In this study, the threshold is set to 90 while the Total *CNF* can vary from 0 to 100. The average and standard deviation of the total CNF for slices without hippocampus for the training set are 40.15 and 15.01, respectively. We have selected the threshold conservatively to ensure no wrong or inaccurate landmark is considered valid, since such an error may cause problems for the final step of the segmentation procedure, the deformable model.

$$CNF = (SuEx\_ICNF + SuHSf\_ICNF + SuInH\_ICNF + InH\_ICNF + ExH\_ICNF + SuH\_ICNF + Sf\_ICNF + ExV\_ICNF + BndSH\_ICNF + BndIH\_ICNF + BndEH\_ICNF + BndSf\_ICNF + BndSV\_ICNF + VntEI\_ICNF)/8$$

The underlying assumption is that applying the proposed search method on slices without hippocampus either produces no results or the results are randomly distributed and so significantly different from what we expect such that the above rules will detect and filter them out. On the other hand, the slices with the hippocampus produce points that are scored above the threshold by the rules.

3. EXPERIMENTAL RESULTS

We evaluate the proposed algorithm by applying it to the T1-weighted MRI's of 10 randomly selected temporal lobe epileptic patients. Fig. 9 illustrates some qualitative results of the hippocampus initialization (first row) and the corresponding final segmentations produced by a deformable model (second row) in sagittal and coronal views for two

patients (two left columns for one patient and two right columns for the other). Quantitatively, we first assess the success of the first phase of the algorithm, the information extraction, during which the landmarks of interest are found. Then we present the assessment of the information analysis phase during which the landmarks are evaluated.

If a point is accurately found on a slice with the landmark of interest (e.g., superior landmark of the hippocampus) or no point is found on the slices without the landmark of interest, then it is considered a success, for the information extraction phase. If a point is found on a slice with no landmark of interest, or the point is not accurately found where the landmark of interest exists, then it is considered a failure. The overall success rate of the information extraction phase was 71.8%.

For the information analysis phase, we consider two measures by which the performance of this phase is assessed: specificity and sensitivity. We calculate the specificity as the ratio of the number of slices with $CNF < 90$ over the number of the slices without hippocampus or with the landmarks of interest inaccurately found. The sensitivity of the information analysis phase is defined as the ratio of the number of the slices with $CNF \geq 90$ over the number of slices the landmarks of interest all accurately found. For these two measures we have obtained very high overall scores of 99.5% (STD: 1.5%) and 98.9% (STD: 3.5%), respectively. This indicates that the proposed rule-based system works very well.

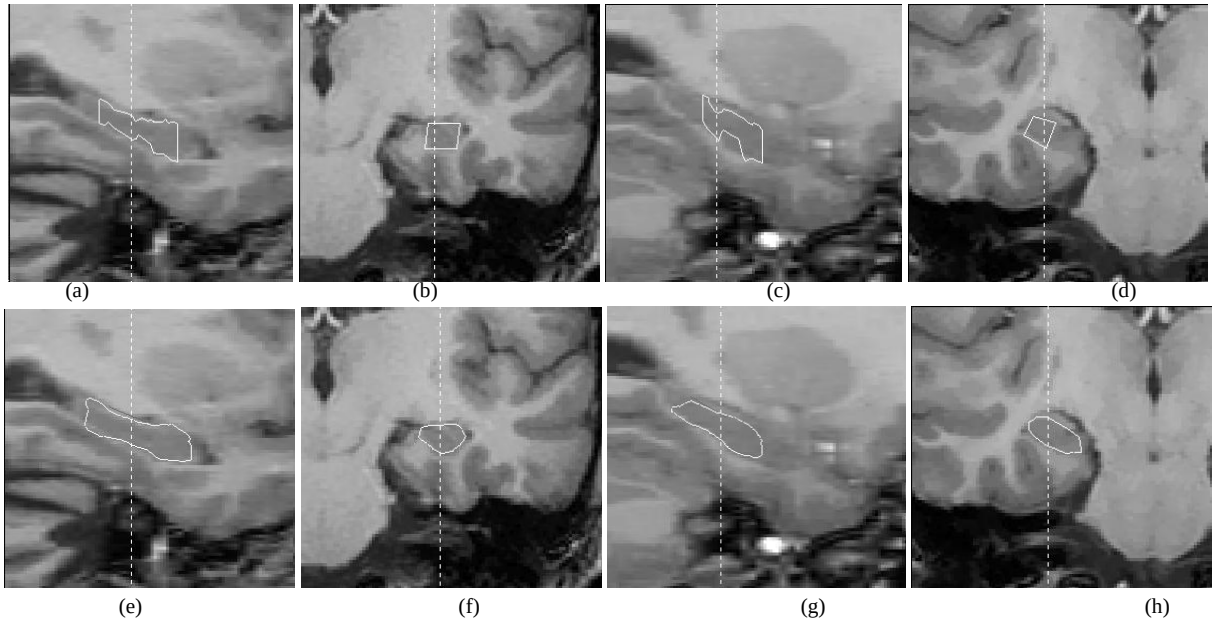

Fig. 9. The hippocampus initialization (initial polygon) and the final segmentation produced by a deformable model when feeding it with the initial polygon. The first row shows the initial polygons and the second row shows the final segmentation results in sagittal and coronal views. The coronal views are perpendicular to the dash-lines shown on the sagittal views and vice versa. The left two columns show the left hippocampus of one patient and the right two columns show the right hippocampus of another patient.

We define the "accuracy" of the algorithm to be the number of the accurate points found for the landmarks of interest divided by the total number of the points found for the landmark of interest on all slices with and without the hippocampus with $CNF \geq 90$. Note that in our experiments, there is no circumstance under which the $CNF \geq 90$ for slices without the hippocampus. The mean, the standard deviation, and the maximum *CNF* for the slices without the hippocampus are 30.8, 19.7, and 87.5, respectively. The outstanding total accuracy of 99.2% with a minimum of 95.83% is far beyond the deformable model demands. There were 8 inaccurate points throughout this experiment where the initial models have 1008 points in total. The inaccuracies mostly caused by the fourth point of the hippocampus (7 out of 8 inaccurate points). Note that we did not estimate a model and there is no rule to examine the fourth point's accuracy in the information analysis phase. This means that the proposed statistical models and evaluation methods failed only once in 1008 cases.

The proposed method did not generate any false alarms. The next measure is the "overall sensitivity," which is the number of detected slices with an accurately identified hippocampus and a $CNF \geq 90$ divided by the total number of slices with the hippocampus. The "overall sensitivity" is 69.7% (STD: 11.51) considering all patients.

The final measure is the overall success rate of the algorithm in performing its ultimate goal: localization of the hippocampus. This measure is calculated as the ratio of the number of correct decisions made by the knowledge-based system divided by the total number of slices being presented to it. A correct decision is producing a $CNF \geq 90$ when the presented slice contains the hippocampus structure or producing a $CNF < 90$ when there is no hippocampus. The overall success rate of the proposed algorithm is 83.3% (STD: 5.0%).

The average model distance of the initial polygon (localization results) from the manually segmented models (as the gold standards) are 2.2 and 2.0 mm with standard deviations of 0.32 and 0.24 for the left and right hippocampi, respectively. The average distance is defined as the average Euclidean minimum distances of the polygon vertices from the surface of the segmented model. The overall similarity of the initial polygons and the manually segmented models are 0.49 and 0.56 with standard deviations of 0.07 and 0.09 for the left and right hippocampi, respectively, when the similarity is define as the ratio of the number of points in the intersection divided by the number of points in the union of the two models.

REFERENCES

1. U. Bick, A. Sprinz, J. Weglage, G. Kurlemann, G. Schuierer, P. E. Peters, "Computer-assisted MRI-volumetry of the amygdala and hippocampus in healthy young adults with a history of febrile convulsions in childhood," *Proceedings of the Computer Assisted Radiology and Surgery (CAR'97)* Editors, H. U. Lemke, K. Inamura, M. W. Vannier, pp.101-4, Amsterdam, The Netherlands, 1998.
2. F. Ohl, T. Michaelis, H. Fujimori, J. Frahm, S. Rensing, E. Fuchs, "Volumetric MRI measurements of the tree shrew hippocampus," *J. Neuroscience Methods*, vol. 88, no. 2, pp. 189-193, May 1999.
3. J. J. Hasenau, *Master of science thesis*, Wayne State University, Detroit, MI, 1997.
4. J. Webb, A. Guimond, P. Eldridge, D. Chadwick, J. Meunier, J. P. Thirion, N. Roberts, "Automatic detection of hippocampal atrophy on magnetic resonance images," *Magn. Reson. Imag.*, vol. 17, no. 8, pp. 1149-1161, Oct. 1999.
5. A. Kelemen, G. Szekely, G. Gerig, "Elastic model-based segmentation of 3-D neuro-radiological data sets," *IEEE Trans. Med. Imag.*, vol. 18, no. 10, pp. 828-839, Oct. 1999.
6. A. Pitiot, A. W. Toga, P. M. Thompson, "Adaptive elastic segmentation of brain MRI via shape-model-guided evolutionary programming," *IEEE Trans Med Imaging*. vol. 21, no. 8, pp. 910-23, Aug 2002.
7. A. Ghanei, H. Soltanian-Zadeh, J. P. Windham, "A 3D deformable surface model for segmentation of objects from volumetric data in medical images," *Computers in Biology and Medicine*, vol. 28, no. 3, pp. 239-253, July 1998.
8. G. E. Christensen, R. D. Rabbitt, M. I. Miller, "Deformable templates using large deformation kinematics," *IEEE Trans. Imag. Proc.*, vol. 5, no. 10, pp. 1435-1447, 1996.
9. A. Davatzikos, B. R.Christos, R. Nick, "Using a deformable surface to obtain a shape representation of the cortex," *IEEE Trans. Med. Imag.*, vol. 15, no. 6, pp. 785-795, 1996.
10. B. C. Vemuri, J. Ye, Y. Chen, C. M. Leonard, "Image registration via level-set motion: applications to atlas-based segmentation," *Med Image Anal.*, vol. 7, no. 1, pp. 1-20, Mar. 2003.
11. Y.-Y. Hsu, N. Schuff, A-T. Du, K. Mark, X. Zhu, D. Hardin, M. W. Weiner, "Comparison of automated and manual MRI volumetry of hippocampus in normal aging and dementia," *J. of Magnetic Resonance Imaging*, vol. 16, pp. 305-310, 2002.
12. B. Fischl, D. H. Salat, E. Busa, M. Albert, M. Dieterich, C. Haselgrove, A. van der Kouwe, R. Killiany, D. Kennedy, S. Klaveness, A. Montillo, N. Makris, B. Rosen, A. M. Dale, "Whole brain segmentation: automated labeling of neuroanatomical structures in the human brain," *Neuron.*, vol. 33, no. 3, pp. 341-55, Jan. 31, 2002.
13. D. Shen, S. Moffat, S. M. Resnick, C. Davatzikos, "Measuring size and shape of the hippocampus in MR images using a deformable shape model," *Neuroimage*, vol. 15, no. 2, pp. 422-434, Feb. 2002.
14. P. M. Thompson, A. W. Toga, "Detection, visualization, and animation of abnormal anatomic structure with a deformable probabilistic brain atlas based on random vector field transformation," *Medical Image Analysis*, vol. 1, no. 4, pp. 271-294, 1997.
15. E. Fisher, R. M. Cothren, J. A. Tkach, T. J. Masaryk, J. F. Cornhill, "Knowledge-based 3D segmentation of the brain in MR images for quantitative multiple sclerosis lesion tracking," *SPIE*, vol. 3034(PT1-2), pp. 19-25, 1997.
16. G. B. Aboutanos, B. M. Dawant, "Automatic brain segmentation and validation: image-based versus atlas-based deformation models," *SPIE*, vol. 3034(PT1-2), pp. 299-310, 1997.
17. O. Migneco, J. Darcourt, J. Benoliel, et al, "Computerized localization of brain structures in single photon computed tomography using a proportional anatomical stereotactic atlas," *Computerized Medical Imaging and Graphics*, vol. 18, no. 6, pp. 413-422, 1994.
18. G. E. Forsythe, M. A. Malcolm, C. B. Moler, *Computer Methods for Mathematical Computations*, Prentice-Hall, 1976.
19. R. C. Gonzalez, R. E. Woods, *Digital Image Processing*, Second Edition, Addison-Wesley, 2002.